

Article

Sensorless Control of Late-Stage Offshore DFIG-WT with FSTP Converters by Using EKF to Ride through Hybrid Faults

Wei Li ¹, Gengyin Li ¹, Kai Ni ^{2,*} , Yihua Hu ²  and Xinhua Li ²

¹ State Key Laboratory of Alternate Electrical Power System with Renewable Energy Sources, North China Electric Power University, Changping District, Beijing 102206, China; li.wei@stategrid.com.br (W.L.); ligy@ncepu.edu.cn (G.L.)

² Department of Electrical Engineering and Electronics, University of Liverpool, Liverpool L69 3GJ, UK; y.hu35@liverpool.ac.uk (Y.H.); xinhua.li@liverpool.ac.uk (X.L.)

* Correspondence: k.ni@student.liverpool.ac.uk; Tel.: +44-07519203720

Received: 23 October 2017; Accepted: 20 November 2017; Published: 23 November 2017

Abstract: A hybrid fault scenario in a late-stage offshore doubly-fed induction generator (DFIG)-based wind turbine (DFIG-WT) with converter open-circuit fault and position sensor failure is investigated in this paper. An extended Kalman filter (EKF)-based sensorless control strategy is utilized to eliminate the encoder. Based on the detailed analysis of the seventh-order dynamic state space model of DFIG, along with the input voltage signals and measured current signals, the EKF algorithm for DFIG is designed to estimate the rotor speed and position. In addition, the bridge arm open circuit in the back-to-back (BTB) power converter of DFIG is taken as a commonly-encountered fault due to the fragility of semiconductor switches. Four-switch three-phase (FSTP) topology-based fault-tolerant converters are employed for post-fault operation by considering the minimization of switching losses and reducing the circuit complexity. Moreover, a simplified space vector pulse width modulation (SVPWM) technique is proposed to reduce the computational burden, and a voltage balancing scheme is put forward to increase the DC-bus voltage utilization rate. Simulation studies are carried out in MATLAB/Simulink2017a (MathWorks, Natick, MA, USA) to demonstrate the validity of the proposed hybrid fault-tolerant strategy for DFIG-WT, with the wind speed fluctuation, measurement noises and grid voltage sag taken into consideration.

Keywords: hybrid fault; doubly-fed induction generator; extended Kalman filter; sensorless control; back-to-back power converter; four-switch three-phase converter

1. Introduction

As one of the most promising renewable energy resources to be used in the world, wind energy has attracted the attention of many researchers [1–4]. With the fast development of power electronics, the fully-rated permanent magnet synchronous generator (PMSG) and partially-rated doubly-fed induction generator (DFIG)-based wind energy conversion systems (WECSs) are the ones mainly used in the wind energy market, since they have the ability of variable-speed constant-frequency (VSCF) operation. The advantages of the small volume and low cost of the back-to-back (BTB) power converter are endowed to DFIG-based wind turbines (DFIG-WTs). However, when these wind turbines approach the end of their lifetime, various types of faults may happen, which result in downtime. Especially for offshore wind applications, where terrible weather conditions and high maintenance cost are present, a longer period of downtime is caused, which leads to more energy and economic losses.

According to [5], although the electronic control system only accounts for around 1% of the total cost of a wind turbine system, 13% of the failures of wind turbines are caused by the faults in

power electronic devices. Although flexible control of DFIG-WT is realized by using power electronic converters, the reliability of the system is deteriorated, owing to the fragility of the semiconductor switches in these converters. In a conventional three-phase AC/DC/AC BTB converter, which consists of a grid-side converter (GSC) and a rotor-side converter (RSC), twelve power switches are applied, with six of them installed in GSC and the other six used in RSC for power regulation. Once a switch is open circuited, the corresponding entire bridge arm will be idle, and the control of the current through this phase will be lost. In order to ride through this kind of fault, three major types of fault-tolerant converter topologies were proposed, including the strategies employing multi-level converters, redundant back-up switches and DC-bus midpoint connection. Considering the merits of minimizing the switching losses and simplifying the circuit configuration, the last option is widely applied, and it is to be utilized in this paper for fault tolerance purposes.

By connecting the DC-bus midpoint to the phase originally connected to the faulty bridge arm, only four switches are to be controlled in this fault-tolerant topology, and the current in the faulty phase is automatically controlled according to the fact that the summation of three-phase currents equals zero. This topology based on four switches is called the four-switch three-phase (FSTP) topology, with respect to its six-switch three-phase (SSTP) counterpart. Despite the simple circuit structure and high reliability of the FSTP topology, the utilization rate of the DC-bus voltage is much lower than that of SSTP, and fluctuation in the upper and lower capacitor voltages exists due to the current in the faulty phase flowing through one of the two DC-link capacitors all the time. In [6], a dq mathematical model of the FSTP voltage source rectifier (VSR) was first derived for control design purposes. Detailed mathematical deduction of the FSTP VSR model was presented, and the “reduced Park transformation” was applied. A comprehensive modelling of a non-redundant fault-tolerant inverter with the method of DC-bus midpoint connection was performed in [7], and the generalized switching functions were proposed. An optimized modulation approach was raised in [8] for the post-fault pulse width modulation (PWM) rectifiers to minimize the capacitor currents so that the current stresses on the capacitors are mitigated. Besides, the modelling, modulation and control of an FSTP rectifier were comprehensively analysed in [9], with a novel linear modulation function proposed. Moreover, the zero voltage distribution in the FSTP converter has been studied to analyse the performance in [10] in terms of the AC current ripple, the common voltage (CMV) and the current stress on the DC-link capacitor. On top of that, the applications of FSTP topology in induction motor drives [11,12], brushless DC (BLDC) motor drives [13,14] and PMSGs [15–17] were extensively investigated. However, there is a rare literature concentrating on improving the performance of FSTP converter-based DFIG-WT. In [18,19], only the faulty case in the GSC was considered, and the other parts of the system were assumed to be intact.

With the purpose of controlling the operation of DFIG-WT, the rotor speed and position information is required. Usually, mechanical and optical sensors such as tachometers and optical encoders are utilized to measure the rotor speed and position [20]. However, with the installation of speed and position sensors, the hardware complexity, cost and the size of the system are increased, and regular maintenance of these sensors is detrimental to the system reliability [21]. In order to avoid these disadvantages, the control algorithm called “sensorless control” was put forward to directly obtain the rotor speed and position by only measuring the voltages and currents [22]. In general, there are two approaches in the sensorless techniques for electrical machines, which are based on signal injection and mathematical modelling. The former approach is usually applied in permanent magnet (PM) machines for zero or low speed scenarios, and its performance is greatly deteriorated when the machine runs at high speed. For induction machine (IM) applications, the corresponding sensorless control methods are usually based on the precise system model.

Different from the other deterministic schemes used for speed/position sensorless control of electrical machines, the Kalman filter (KF) [23] is a kind of stochastic approach. In terms of nonlinear systems such as IMs, PM machines and doubly-fed induction machines (DFIMs), an updated version of the KF stochastic algorithm called the EKF is usually applied for estimating the non-measured

parts of the system [24,25]. Since EKF has good robustness to disturbances such as process and measurement noises in a complicated nonlinear system, the reliability of this method can be ensured even if uncertainties are induced in the estimation process [24,25].

An optimized EKF was proposed by using a real-coded genetic algorithm for properly selecting the noise covariance and weight matrices to guarantee filter stability and accuracy in speed estimation of an IM drive in [26]. In [27], the EKF algorithms were applied in speed sensorless control of IMs by combining field-oriented control (FOC) and direct-torque control (DTC). Additionally, a braided EKF was proposed for sensorless control of IMs in [28], and challenging parameter and load variations in a wide speed range were considered to verify the algorithm. The convergence analysis of EKF for sensorless control of IM was presented in [29]. In spite of a number of research works and applications of EKF algorithms in IMs, there is a rare literature focusing on speed and position sensorless control of DFIGs by using EKF. The research on the EKF algorithm for DFIM was first conducted in [30], and a suitable model was proposed for estimating the rotor position, speed and mechanical torque of DFIG. In [31], an EKF was proposed as the rotor position estimator, and the observability of the DFIG was analysed. In [32], a comprehensive analysis of the performance of an EKF was carried out for the non-augmented, partially-augmented and augmented state models of DFIG, respectively, and the best performance was obtained when applying the proposed augmented state estimator. Furthermore, a sensorless optimal power control of brushless DFIG (BDFIG) based on EKF was investigated in [33]. However, all these literature works mentioned only took one faulty scenario into consideration, which may be ineffective for post-fault operation of DFIG at the late stage of service time.

This paper investigates the hybrid fault-tolerant operation of late-stage offshore DFIG-WT, where open-circuit faults in the bridge arms of the BTB converter and position encoder failure occur simultaneously, which has not been researched before. The EKF algorithm is combined with the FSTP BTB converter in a DFIG-WT to ride through the hybrid fault case mentioned. The seventh-order dynamic model of DFIG is deeply analysed, and the robustness of EKF to measurement noises is proven in the sensorless control process. In addition, a simplified space vector PWM (SVPWM) technique and a voltage balancing control scheme are proposed for the FSTP BTB converter to improve the post-fault performance of DFIG-WT without complicating the control process. The hybrid fault scenario considered in this paper is displayed in Figure 1.

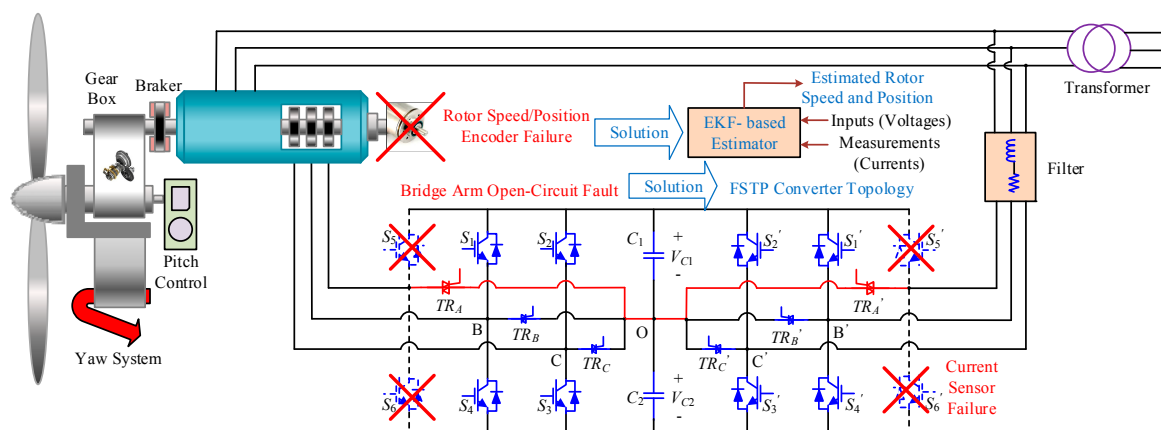


Figure 1. Rotor position encoder failure and bridge arm open-circuit fault in doubly-fed induction generator-based wind turbine (DFIG-WT). FSTP, four-switch three-phase.

The organization of the paper is shown as follows: In Section 2, the DFIG dynamic model is explained. The EKF estimator for DFIG is presented in Section 3. Then, the configuration, modulation and control of the FSTP BTB converter are illustrated in Section 4. After that, the sensorless control strategy for an FSTP BTB converter-based DFIG-WT by using the EKF algorithm is discussed in

Section 5. In Section 6, the simulation results are shown with descriptions and analysis. Finally, the conclusion is given in Section 7.

2. DFIG Dynamic Model

Similar to other three-phase AC machines, the DFIG model expressed in a three-phase coordination system is complex, since it contains the characteristics of high order, multiple variables, nonlinearity, strong coupling and time variations. In this case, it is difficult to control the operation of the system. In order to effectively control the active and reactive power of DFIG, it is feasible to implant the vector control (VC) technique. The relationships among the three-phase stationary reference frame (ABC), three-phase rotor reference frame (abc), two-phase stationary reference frame ($\alpha\beta_s$), two-phase rotor reference frame ($\alpha\beta_r$) and two-phase arbitrary rotating reference frame (dq) are illustrated in Figure 2.

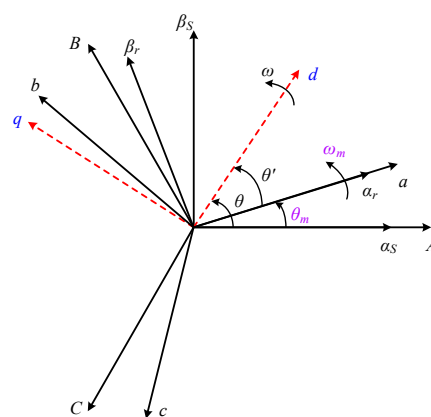


Figure 2. Relationships among reference frames.

By transforming the three-phase currents to an arbitrary rotating two-phase reference frame, namely the dq reference frame, the independent control of the active and reactive power can be realized by controlling the current components on the d - and q -axis. In a dq synchronous reference frame, the dynamic model of DFIG can be expressed by the following equations.

$$\begin{cases} \mathbf{v}_s = R_s \mathbf{i}_s + \frac{d\boldsymbol{\varphi}_s}{dt} + j\omega_s \boldsymbol{\varphi}_s \\ \mathbf{v}_r = R_r \mathbf{i}_r + \frac{d\boldsymbol{\varphi}_r}{dt} + j\omega_{slip} \boldsymbol{\varphi}_r \end{cases} \quad (1)$$

$$\begin{cases} \boldsymbol{\varphi}_s = L_s \mathbf{i}_s + L_m \mathbf{i}_r \\ \boldsymbol{\varphi}_r = L_m \mathbf{i}_s + L_r \mathbf{i}_r \end{cases} \quad (2)$$

$$T_e = n_p L_m (i_{rd} i_{sq} - i_{rq} i_{sd}) \quad (3)$$

$$T_e - T_L = \frac{J}{n_p} \frac{d\omega_m}{dt} \quad (4)$$

Equations (1)–(4) are the voltage equations, flux equations, electromagnetic torque equation and kinetic equation, respectively.

From Figure 2, it can be seen that the information of the rotor speed ω_m and position θ_m is of paramount importance since it is directly related to the transformation of the rotor variables to the dq frame. In the normal case, a speed or position encoder is utilized for obtaining the values of ω_m and θ_m . In order to increase the system reliability, the encoder is eliminated in this paper, and a seventh-order state space model of DFIG is established for designing the estimator of the rotor speed and position to realize sensorless control. The state $\mathbf{x}(t)$ consists of the dq stator and rotor currents, rotor angular speed, rotor position and the mechanical torque. The stator currents in the $\alpha\beta_s$ reference frame and the

rotor currents in the $\alpha\beta_r$ reference frame can be directly measured, and the $\alpha\beta$ stator and rotor voltages can be used as the inputs of the system. The state $\mathbf{x}(t)$, measurements $\mathbf{y}(t)$ and inputs $\mathbf{u}(t)$ of the DFIG system can be expressed as shown below.

$$\begin{aligned} \mathbf{x}(t) &= [i_{sd}(t) \quad i_{sq}(t) \quad i_{rd}(t) \quad i_{rq}(t) \quad \omega_m(t) \quad \theta_m(t) \quad T_m(t)]^T \\ \mathbf{y}(t) &= [i_{s\alpha}(t) \quad i_{s\beta}(t) \quad i_{r\alpha}(t) \quad i_{r\beta}(t)]^T \\ \mathbf{u}(t) &= [v_{s\alpha}(t) \quad v_{s\beta}(t) \quad v_{r\alpha}(t) \quad v_{r\beta}(t)]^T \end{aligned} \quad (5)$$

The electrical variables of DFIG are in the dq synchronous reference frame, whereas those in the inputs and measurements are oriented in the $\alpha\beta$ stationary reference frame, and the transformation between the reference frames is dependent on the rotor position θ_m , leading to the nonlinearity of the DFIG model. Under this circumstance, the state variable model is expressed in the general form with the rate of change in the state $d\mathbf{x}(t)/dt$, which can be regarded as the process function $\mathbf{f}(\mathbf{x}(t), \mathbf{u}(t))$ as shown in (6).

$$\mathbf{f}(\mathbf{x}(t), \mathbf{u}(t)) = \begin{bmatrix} \frac{1}{\sigma L_s L_r} [L_r v_{sd} - L_r R_s i_{sd} - L_m v_{rd} + L_m R_r i_{rd} + \omega_m L_m L_r i_{rq} + (\omega_s L_s L_r - \omega_{slip} L_m^2) i_{sq}] \\ \frac{1}{\sigma L_s L_r} [L_r v_{sq} - L_r R_s i_{sq} - L_m v_{rq} + L_m R_r i_{rq} - \omega_m L_m L_r i_{rd} - (\omega_s L_s L_r - \omega_{slip} L_m^2) i_{sd}] \\ \frac{1}{\sigma L_s L_r} [L_s v_{rd} - L_s R_r i_{rd} - L_m v_{sd} + L_m R_s i_{sd} - \omega_m L_m L_s i_{sq} - (\omega_s L_m^2 - \omega_{slip} L_s L_r) i_{rq}] \\ \frac{1}{\sigma L_s L_r} [L_s v_{rq} - L_s R_r i_{rq} - L_m v_{sq} + L_m R_s i_{sq} + \omega_m L_m L_s i_{sd} + (\omega_s L_m^2 - \omega_{slip} L_s L_r) i_{rd}] \\ \frac{1}{J} [\frac{3}{2} n_p L_m (i_{rd} i_{sq} - i_{rq} i_{sd}) - T_m] \\ \omega_m \\ 0 \end{bmatrix} \quad (6)$$

where σ is the leakage coefficient, and it can be expressed as:

$$\sigma = 1 - \frac{L_m^2}{L_s L_r} \quad (7)$$

The measurement matrix of the system can be derived as

$$\mathbf{h}(\mathbf{x}(t)) = \begin{bmatrix} \cos(\theta_s) i_{sd} - \sin(\theta_s) i_{sq} \\ \sin(\theta_s) i_{sd} + \cos(\theta_s) i_{sq} \\ \cos(\theta_{slip}) i_{rd} - \sin(\theta_{slip}) i_{rq} \\ \sin(\theta_{slip}) i_{rd} + \cos(\theta_{slip}) i_{rq} \end{bmatrix} \quad (8)$$

3. EKF Estimator for DFIG

A KF is usually applicable for estimating the state variables in a linear system, which is a stochastic approach and takes the system and measurement noises into account. The optimal time-varying observer gain $\mathbf{K}(t)$ is obtained to minimize the estimation error, considering the process and measurement noises.

3.1. Continuous DFIG State Space Nonlinear Model

For a continuous DFIG state space model, which is endowed with nonlinearity due to the presence of coordinate system transformation, an approximated linear system that evolves from the nonlinear DFIG model by using EKF algorithm is formulated to estimate the state variables. The continuous state space model of DFIG in the general form can be expressed as shown below.

$$\frac{d\mathbf{x}(t)}{dt} = \mathbf{f}(\mathbf{x}(t), \mathbf{u}(t)) + \mathbf{w}(t)(\text{system}), \quad (9)$$

$$\mathbf{y}(t) = \mathbf{h}(\mathbf{x}(t)) + \mathbf{v}(t)(\text{measurement}), \quad (10)$$

In the dynamic process of the system $\mathbf{x}(t)$ and the measurement output vector $\mathbf{y}(t)$, white noises $\mathbf{w}(t)$ and $\mathbf{v}(t)$ that obey a Gaussian distribution are considered to indicate the model uncertainties in the system and the external disturbances in the measurement process, respectively. By minimizing the covariance of the estimation error, the optimal state estimation can be obtained. The covariance matrices of $\mathbf{w}(t)$ and $\mathbf{v}(t)$ are \mathbf{Q} and \mathbf{R} , respectively, and they do not have a correlation with each other.

$$\mathbf{Q} = \text{cov}(\mathbf{w}) = E\{\mathbf{w}\mathbf{w}^T\}, \quad (11)$$

$$\mathbf{R} = \text{cov}(\mathbf{v}) = E\{\mathbf{v}\mathbf{v}^T\}, \quad (12)$$

3.2. Discretization of the DFIG State Space Nonlinear Model

Based on the Euler approximation [34], the discretized model of the DFIG state space nonlinear model can be derived by introducing the concept of sampling time T_s . The discrete model obtained based on (9) and (10) is applicable for implementing EKF algorithms, since the state variables at the next time step can be predicted and updated in this case. The state variable discretization process using the forward-Euler approximation principle can be expressed as:

$$\frac{d\mathbf{x}}{dt} \approx \frac{\mathbf{x}(k+1) - \mathbf{x}(k)}{T_s}, \quad (13)$$

In this equation, k and $(k+1)$ represent the present and next time steps for the state, respectively. Specifically, the electrical variables in the next state can be displayed as shown below.

$$\begin{cases} i_{sd}(k+1) = i_{sd}(k) + T_s \frac{di_{sd}}{dt} \Big|_k \\ i_{sq}(k+1) = i_{sq}(k) + T_s \frac{di_{sq}}{dt} \Big|_k \\ i_{rd}(k+1) = i_{rd}(k) + T_s \frac{di_{rd}}{dt} \Big|_k \\ i_{rq}(k+1) = i_{rq}(k) + T_s \frac{di_{rq}}{dt} \Big|_k \end{cases}, \quad (14)$$

The precision of model discretization by applying this method is dependent on the value of T_s , and a more accurate approximation is available for the mechanical rotor speed/position by Taylor series expansion [35,36], and the discrete expressions for ω_m and θ_m are illustrated as:

$$\begin{aligned} \omega_m(k+1) = \omega_m(k) + T_s \frac{d\omega_m}{dt} \Big|_k + \frac{T_s^2}{2} \left(\frac{d\omega_m}{dt} \frac{di_{sd}}{dt} \Big|_k \frac{di_{sd}}{dt} \Big|_k \right. \\ \left. + \frac{d\omega_m}{dt} \frac{di_{sq}}{dt} \Big|_k + \frac{d\omega_m}{dt} \frac{di_{rd}}{dt} \Big|_k + \frac{d\omega_m}{dt} \frac{di_{rq}}{dt} \Big|_k \right) \end{aligned}, \quad (15)$$

$$\theta_m(k+1) = \theta_m(k) + T_s \omega_m(k) + \frac{T_s^2}{2} \frac{d\omega_m}{dt} \Big|_k, \quad (16)$$

As the inertia of wind turbine is relatively large and the time step T_s is usually in ms or even μs , the mechanical torque at the next time step is regarded the same as the present one, which satisfies the following equation.

$$T_m(k+1) = T_m(k), \quad (17)$$

Therefore, the discrete process function of the state can be derived as shown below.

$$\mathbf{F}(\mathbf{x}(k), \mathbf{u}(k)) = \begin{bmatrix} i_{sd}(k) + \frac{T_s}{\sigma L_s L_r} [L_r v_{sd} - L_r R_s i_{sd} - L_m v_{rd} + L_m R_r i_{rd} + \omega_m L_m L_r i_{rq} + (\omega_s L_s L_r - \omega_{slip} L_m^2) i_{sq}] |k \\ i_{sq}(k) + \frac{T_s}{\sigma L_s L_r} [L_r v_{sq} - L_r R_s i_{sq} - L_m v_{rq} + L_m R_r i_{rq} - \omega_m L_m L_r i_d - (\omega_s L_s L_r - \omega_{slip} L_m^2) i_{sd}] |k \\ i_{rd}(k) + \frac{T_s}{\sigma L_s L_r} [L_s v_{rd} - L_s R_r i_{rd} - L_m v_{sd} + L_m R_s i_{sd} - \omega_m L_m L_s i_{sq} - (\omega_s L_m^2 - \omega_{slip} L_s L_r) i_{rq}] |k \\ i_{rq}(k) + \frac{T_s}{\sigma L_s L_r} [L_s v_{rq} - L_s R_r i_{rq} - L_m v_q + L_m R_s i_{sd} q + \omega_m L_m L_s i_{sd} + (\omega_s L_m^2 - \omega_{slip} L_s L_r) i_d] |k \\ \omega_m(k) + \frac{T_s}{J} [\frac{3}{2} n_p L_m (i_{rd} i_{sq} - i_{rq} i_{sd}) |k - T_m(k)] + \frac{3 T_s^2}{4 J} n_p L_m (i_{sq} \frac{di_{rq}}{dt} + i_{rq} \frac{di_{sq}}{dt} - i_{sd} \frac{di_{rq}}{dt} - i_{rq} \frac{di_{sd}}{dt}) |k \\ \theta_m(k) + T_s \omega_m(k) + \frac{T_s^2}{2 J} [\frac{3}{2} n_p L_m (i_{rd} i_{sq} - i_{rq} i_{sd}) |k - T_m(k)] \\ T_m(k) \end{bmatrix}, \quad (18)$$

The measurement matrix in the discrete format can be obtained as:

$$\mathbf{H}(\mathbf{x}(k)) = \begin{bmatrix} \cos(\theta_s(k)) i_{sd}(k) - \sin(\theta_s(k)) i_{sq}(k) \\ \sin(\theta_s(k)) i_{sd}(k) + \cos(\theta_s(k)) i_{sq}(k) \\ \cos(\theta_{slip}(k)) i_{rd}(k) - \sin(\theta_{slip}(k)) i_{rq}(k) \\ \sin(\theta_{slip}(k)) i_{rd}(k) + \cos(\theta_{slip}(k)) i_{rq}(k) \end{bmatrix}, \quad (19)$$

Then, the following discrete model is achieved.

$$\mathbf{x}(k + 1) = \mathbf{F}(\mathbf{x}(k), \mathbf{u}(k)) + \mathbf{w}(k)(\text{system}), \quad (20)$$

$$\mathbf{y}(k) = \mathbf{H}(\mathbf{x}(k)) + \mathbf{v}(k)(\text{measurement}), \quad (21)$$

3.3. EKF Algorithm

There are two main stages in the EKF algorithm, namely the prediction and update stages. In the EKF algorithm, the states are predicted, while the inputs and measurements are directly obtained and are deterministic.

In the prediction process, the estimated value at the next time step is derived as:

$$\hat{\mathbf{x}}(k + 1|k) = \mathbf{F}(\hat{\mathbf{x}}(k|k), \mathbf{u}(k)), \quad (22)$$

The state estimate error covariance matrix \mathbf{P} is predicted by:

$$\mathbf{P}(k + 1|k) = \mathbf{\Phi}(k) \mathbf{P}(k|k) \mathbf{\Phi}(k)^T + \mathbf{Q}, \quad (23)$$

where $\mathbf{\Phi}(k)$ is the Jacobi matrix derived by linearizing the system around the estimated operating point.

$$\mathbf{\Phi}(k) = \left[\frac{d\mathbf{F}}{d\mathbf{x}} \right]_{(\hat{\mathbf{x}}(k|k), \mathbf{u}(k))}, \quad (24)$$

In the update procedure, the correction term is calculated to compensate for the errors induced in the prediction process. The error between the real measurement and the measurement based on the predicted state is derived as:

$$\mathbf{e}(k) = \mathbf{y}(k) - \mathbf{H}(\hat{\mathbf{x}}(k|k - 1)), \quad (25)$$

The predicted state variables are corrected by dealing with the error with the Kalman gain matrix $\mathbf{K}(k)$.

$$\hat{\mathbf{x}}(k|k) = \hat{\mathbf{x}}(k|k - 1) + \mathbf{K}(k) \mathbf{e}(k), \quad (26)$$

The calculation of the Kalman gain matrix is illustrated as:

$$\mathbf{K}(k) = \mathbf{P}(k|k - 1) \mathbf{C}(k)^T [\mathbf{C}(k) \mathbf{P}(k|k - 1) \mathbf{C}(k)^T + \mathbf{R}]^{-1}, \quad (27)$$

where $C(k)$ is the Jacobi matrix for linearizing the measurement matrix H around the estimated operating point according to the predicted state variables.

$$C(k) = \left[\frac{dH}{dx} \right] (\hat{x}(k|k-1)), \tag{28}$$

The update of the state estimate error covariance matrix P is accomplished by:

$$P(k|k) = [I - K(k)C(k)]P(k|k-1), \tag{29}$$

where I is a unit matrix. The EKF algorithm for a seventh-order DFIG model is displayed in Figure 3.

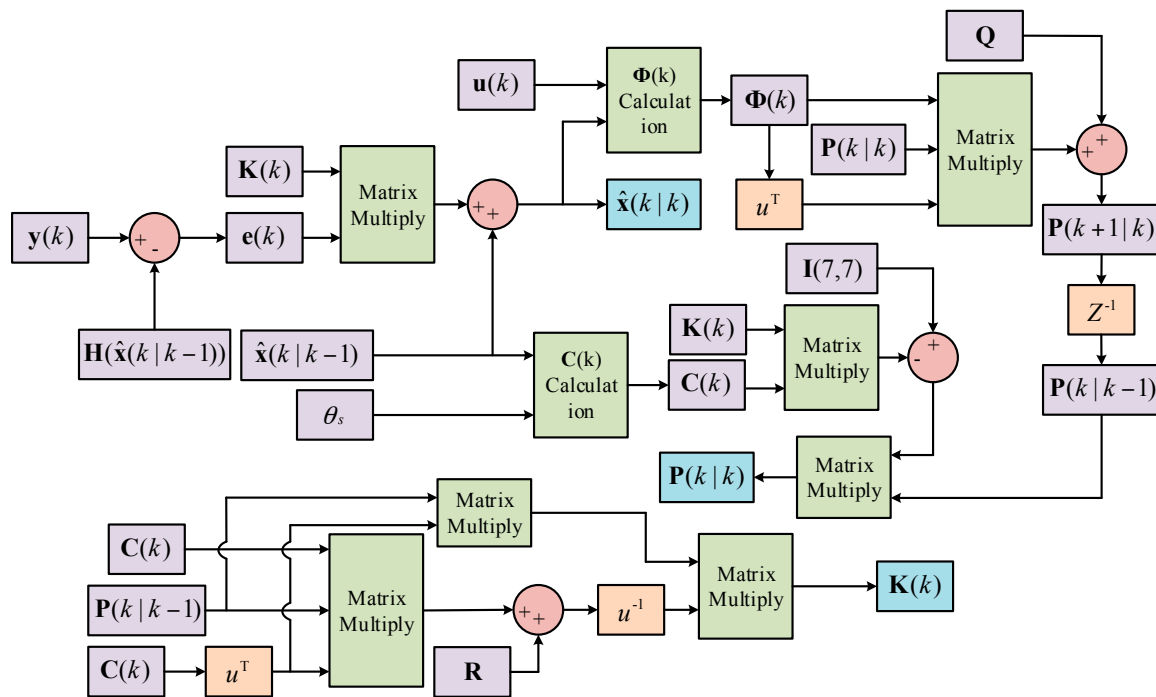


Figure 3. EKF algorithm for the seventh-order DFIG model.

4. FSTP BTB Converter

The faulty case of one bridge arm open circuit in the GSC or RSC caused by the breakdown of a power electronic switch in the converter is taken into consideration, and the FSTP converter is utilized as a fault-tolerant solution without switch redundancy for the post-fault operation of DFIG-WT. Considering balanced three-phase voltage sources and three-phase loads, the open-circuit faults in all three phases can be regarded as identical [37].

4.1. Reconfiguration from SSTP to FSTP

In this paper, taking the faulty case in Phase A of RSC and that of GSC as examples, the reconfiguration of the three-phase BTB power electronic converter in DFIG-WT is displayed in Figure 4.

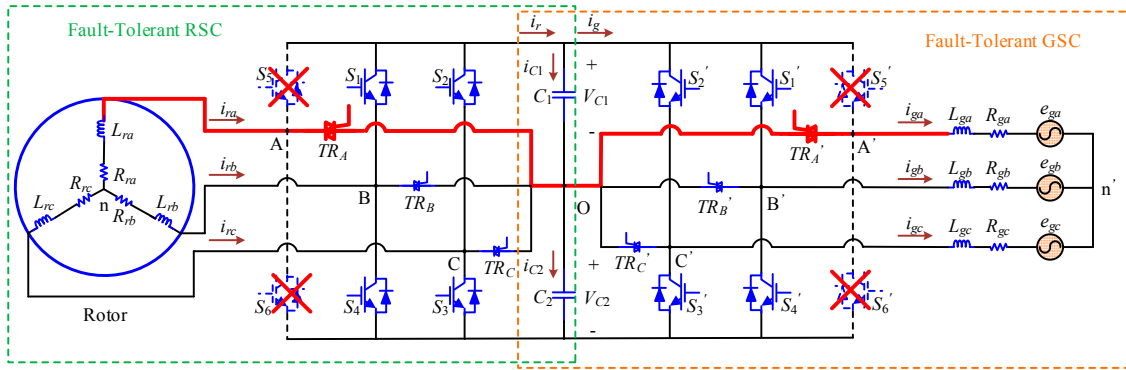


Figure 4. Reconfiguration from the six-switch three-phase (SSTP)- to FSTP-based back-to-back (BTB) converter topology.

In Figure 4, n and n' are the neutral points of the three-phase load and voltage sources, respectively. S_1 – S_6 and S_1' – S_6' are the power switches for the RSC and GSC, respectively. In order to implement the FSTP topology, the midpoint of the DC-bus is connected to the phase with the fault, and the capacitances of the upper and lower capacitors are assumed to be the same ($C_1 = C_2 = C_{DC}$) for voltage balancing purposes. After the open-circuit fault in S_5 or S_6 breaks down, Phase A is directly connected to the DC-bus midpoint O by activating the triac TR_A , and the situation is similar for GSC. Therefore, the controllable switches in this FSTP-based BTB converter are S_1 – S_4 and S_1' – S_4' , and the switching states are defined by the switching functions S_b and S_c (S_b' and S_c'), which are assigned the value of one or zero. The definition of switching states for an FSTP converter is shown in Table 1.

Table 1. Definition of switching states for the rotor-side converter (RSC) (Add ' for GSC).

S_b	S_c	Description	Vector
0	0	S_1 off and S_4 on; S_2 off and S_3 on	V_{00}
0	1	S_1 off and S_4 on; S_2 on and S_3 off	V_{01}
1	0	S_1 on and S_4 off; S_2 off and S_3 on	V_{10}
1	1	S_1 on and S_4 off; S_2 on and S_3 off	V_{11}

4.2. Modelling of the FSTP Converter

The three-phase grid-side and rotor-side AC voltages $v_{A'}$, $v_{B'}$, $v_{C'}$ and v_A , v_B , v_C can be calculated according to the upper and lower capacitor voltages V_{dc1} , V_{dc2} and the switching functions S_b and S_c (S_b' and S_c'), and the relationships are illustrated in the following equations.

$$\begin{cases} v_A = \frac{1}{3}V_{dc1}(-S_b - S_c) + \frac{1}{3}V_{dc2}(2 - S_b - S_c) \\ v_B = \frac{1}{3}V_{dc1}(2S_b - S_c) + \frac{1}{3}V_{dc2}(2S_b - S_c - 1) \\ v_C = \frac{1}{3}V_{dc1}(2S_c - S_b) + \frac{1}{3}V_{dc2}(2S_c - S_b - 1) \end{cases}, \quad (30)$$

$$\begin{cases} v_{A'} = \frac{1}{3}V_{dc1}(-S_b' - S_c') + \frac{1}{3}V_{dc2}(2 - S_b' - S_c') \\ v_{B'} = \frac{1}{3}V_{dc1}(2S_b' - S_c') + \frac{1}{3}V_{dc2}(2S_b' - S_c' - 1) \\ v_{C'} = \frac{1}{3}V_{dc1}(2S_c' - S_b') + \frac{1}{3}V_{dc2}(2S_c' - S_b' - 1) \end{cases}, \quad (31)$$

According to different switching states, the expressions of the three-phase AC voltages are displayed in Table 2.

Table 2. Three-phase AC voltages of the FSTP converter.

$S_b (S_b')$	$S_c (S_c')$	Vector	$v_A (v_{A'})$	$v_B (v_{B'})$	$v_C (v_{C'})$	v_α	v_β
0	0	V_{00}	$\frac{2V_{dc2}}{3}$	$-\frac{V_{dc2}}{3}$	$-\frac{V_{dc2}}{3}$	$\frac{2V_{dc2}}{3}$	0
1	0	V_{10}	$\frac{V_{dc2}-V_{dc1}}{3}$	$\frac{2V_{dc1}+V_{dc2}}{3}$	$-\frac{V_{dc1}+2V_{dc2}}{3}$	$\frac{V_{dc2}-V_{dc1}}{3}$	$\frac{\sqrt{3}(V_{dc1}+V_{dc2})}{3}$
1	1	V_{11}	$-\frac{2V_{dc1}}{3}$	$\frac{V_{dc1}}{3}$	$\frac{V_{dc1}}{3}$	$-\frac{2V_{dc1}}{3}$	0
0	1	V_{01}	$\frac{V_{dc2}-V_{dc1}}{3}$	$-\frac{V_{dc1}+2V_{dc2}}{3}$	$\frac{2V_{dc1}+V_{dc2}}{3}$	$\frac{V_{dc2}-V_{dc1}}{3}$	$\frac{\sqrt{3}(V_{dc1}+V_{dc2})}{3}$

As is shown in Figure 4, DFIG-WT operates in the supersynchronous operational mode, and both the stator and rotor feed power to the grid. In this case, the expressions of the capacitor currents i_{C1} and i_{C2} can be derived from either the RSC or GSC side.

$$\begin{cases} i_{C1} = S_b i_{rb} + S_c i_{rc} - i_g \\ i_{C2} = (S_b - 1) i_{rb} + (S_c - 1) i_{rc} - i_g \end{cases} \quad (\text{from RSC side}), \quad (32)$$

$$\begin{cases} i_{C1} = -(S_b i_{gb} + S_c i_{gc}) + i_r \\ i_{C2} = (1 - S_b) i_{gb} + (1 - S_c) i_{gc} + i_r \end{cases} \quad (\text{from GSC side}), \quad (33)$$

Since there is no additional wire connecting to the neutral points n and n' , the following conditions are satisfied.

$$\begin{cases} i_{ra} + i_{rb} + i_{rc} = 0 \\ i_{ga} + i_{gb} + i_{gc} = 0 \end{cases} \quad (34)$$

Therefore, the currents in the faulty phases A and A' can be calculated according to Kirchhoff current laws as shown below.

$$i_{ra} - i_{ga} = i_{C2} - i_{C1} = C_{DC} \frac{d(V_{dc2} - V_{dc1})}{dt}, \quad (35)$$

The voltage difference ΔV between V_{dc1} and V_{dc2} can be derived as:

$$\Delta V = V_{dc2}(t) - V_{dc1}(t) = \frac{1}{C_{DC}} \int_0^t (i_{ra} - i_{ga}) dt + V_{dc2}(0) - V_{dc1}(0), \quad (36)$$

where $V_{dc1}(0)$ and $V_{dc2}(0)$ are the initial values for the upper and lower capacitor voltages, which are assumed to be $V_{DC}/2$ for simplicity.

According to Equations (30)–(36), the DC-link voltage difference can be compensated by adding compensating current components to the difference between the current flows through the faulty phases for both the GSC and RSC. Therefore, the FSTP BTB control system can still work when bridge arm open-circuit faults happen simultaneously in both converters. However, this is quite a rare case, and the FSTP topology is a temporary solution to ensure that the wind turbine can continue working to reduce the times of maintenance; it is very unlikely that another bridge arm breaks down during this period. Then, in a scheduled maintenance process, all the wind turbines in the wind farm will be repaired. Moreover, if FSTP topologies are used in both the RSC and GSC, the control process will be rather complicated. In this case, the innate advantages of DFIG are lost, which exceeds the scope of this paper.

4.3. Proposed SVPWM Technique for the FSTP Converter

In an SSTP converter, there are eight basic voltage vectors, which are obtained according to the switching states of the power switches in all three bridge arms, and among them, there are two zero voltage vectors (V_{000} , V_{111}) to compensate for the remaining time in a switching time period T_{sw} . However, in an FSTP converter, owing to the absence of the faulty bridge arm (Phases A and A' in this paper), the number of controllable power switches is four, and they contribute to only four basic voltage

vectors; no zero voltage vector is intrinsically available. Under such a circumstance, the equivalent zero voltage vectors are to be synthesized by allocating the remaining time in a switching period to the vectors with opposite components. The comparison between the space vector allocations for SSTP and FSTP converters is displayed in Figure 5.

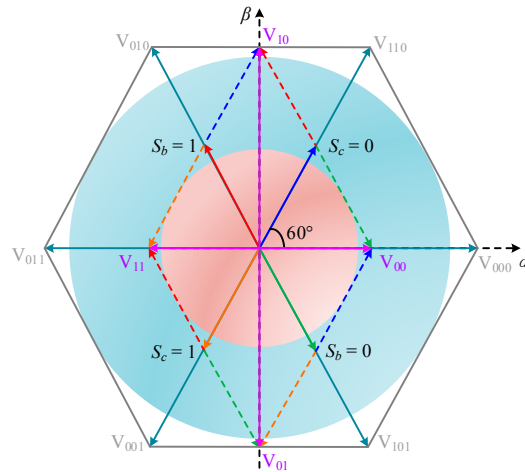


Figure 5. Space vector allocations for the SSTP and FSTP converters.

It can be seen from Figure 5 that with the absence of the switching function S_a , the overall area covered by the locus of the output voltage vector is reduced to one-fourth of the original one, and the utilization rate of the DC-bus voltage is halved. In addition, the amplitudes of the four basic voltage vectors are not the same, where the amplitude of V_{10}/V_{01} is $\sqrt{3}$ times that of V_{00}/V_{11} . However, the statements above only apply to the case when the upper and lower DC-link capacitor voltages are the same. When there is a voltage deviation between V_{dc1} and V_{dc2} , the allocation of space vectors for an FSTP converter is displayed in Figure 6.

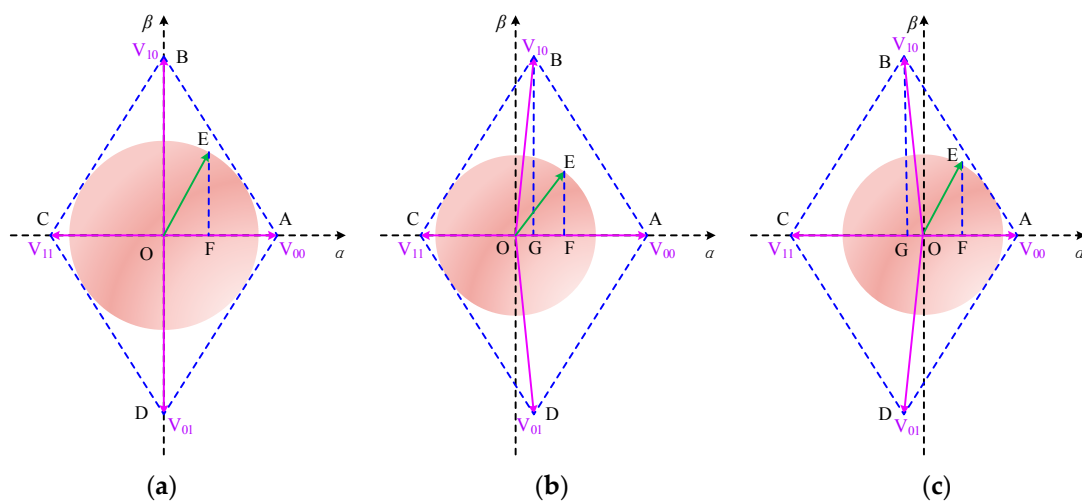


Figure 6. Space vector allocation for an FSTP converter with (a) $V_{dc1} = V_{dc2}$ (b) $V_{dc1} < V_{dc2}$ (c) $V_{dc1} > V_{dc2}$.

When there is a difference between V_{dc1} and V_{dc2} , the discharging time for the capacitors C_1 and C_2 is not the same, which results in different amplitudes of V_{00} and V_{11} , and the orientations of V_{10} and V_{01} are changed as shown in Figure 6b,c. Under these situations, the circular area becomes smaller, which is undesirable since it indicates a decreased DC-bus voltage utilization rate. Moreover, in order to minimize the switching losses and current ripples during the zero voltage vector synthesis process,

the two voltage vectors with smaller amplitudes (V_{00} and V_{11}) are utilized. The situation in Figure 6b can be taken as a general case for analysing the duty ratio for each switching state in Sector I (the area of ΔOAB).

OE represents the output voltage vector, and the α and β components of it are depicted as **OF** and **FE**; they can be calculated as

$$\begin{cases} \mathbf{OF} = \mathbf{OA} \times d_{00} + \mathbf{OC} \times d_{11} + \mathbf{OG} \times d_{10} \\ \mathbf{FE} = \mathbf{GB} \times d_{10} \end{cases}, \quad (37)$$

The vectors, **OE**, **OF** and **FE** can also be expressed as:

$$\begin{cases} \mathbf{OE} = m\mathbf{V}_m \\ \mathbf{OF} = \mathbf{v}_{A_ref} \\ \mathbf{FE} = \frac{\mathbf{v}_{B_ref} - \mathbf{v}_{C_ref}}{\sqrt{3}} \end{cases}, \quad (38)$$

where \mathbf{v}_{A_ref} , \mathbf{v}_{B_ref} and \mathbf{v}_{C_ref} are the reference voltage vectors of the three-phase AC voltages.

$$\begin{cases} \mathbf{v}_{A_ref}^* = V_m \cos(\theta_s) \\ \mathbf{v}_{B_ref}^* = V_m \cos(\theta_s - \frac{2\pi}{3}) \angle \frac{2\pi}{3} \\ \mathbf{v}_{C_ref}^* = V_m \cos(\theta_s + \frac{2\pi}{3}) \angle \frac{4\pi}{3} \end{cases}, \quad (39)$$

In addition, the sum of the duty ratios for all the basic voltage vectors in a switching period is one. By taking this condition and (37)–(39) into account, the values of d_{00} , d_{10} and d_{11} can be calculated as:

$$\begin{cases} d_{00} = \frac{V_{dc1} + v_{A_ref} - v_{B_ref}}{V_{dc}} \\ d_{10} = \frac{v_{B_ref} - v_{C_ref}}{V_{dc}} \\ d_{11} = \frac{V_{dc2} + v_{C_ref} - v_{A_ref}}{V_{dc}} \end{cases}, \quad (40)$$

Then, the equivalent duty ratios for the healthy bridge arms are calculated as:

$$\begin{cases} d_b = d_{10} + d_{11} = \frac{V_{dc2} + v_{B_ref} - v_{A_ref}}{V_{dc}} \\ d_c = d_{11} = \frac{V_{dc2} + v_{C_ref} - v_{A_ref}}{V_{dc}} \end{cases}, \quad (41)$$

When the output voltage vector $\mathbf{Vo} = m\mathbf{V}_m$ is located in the other sectors, the expressions for d_b and d_c remain the same, which indicates that sector identification is not required and the complexity of the modulation technique is greatly reduced. In this simplified SVPWM technique, the duty ratio of the equivalent zero voltage vector d_0 can also be obtained, which has different expressions when \mathbf{Vo} is in different sectors. The expressions for d_0 are shown in Table 3.

Table 3. Duty ratios of the equivalent zero voltage vectors.

	Sector I	Sector II	Sector III	Sector IV
d_0	$\frac{V_{dc2} + v_{C_ref} - v_{A_ref}}{V_{dc}}$	$\frac{V_{dc1} + v_{A_ref} - v_{B_ref}}{V_{dc}}$	$\frac{V_{dc1} + v_{A_ref} - v_{C_ref}}{V_{dc}}$	$\frac{V_{dc2} + v_{B_ref} - v_{A_ref}}{V_{dc}}$

5. Sensorless Control of the FSTP Converter-Based DFIG-WT with the EKF Estimator

On the one hand, the control of DFIG-WT is actually the control of the RSC, which accomplishes the regulation of the active and reactive power output. On the other hand, in order to provide steady DC-bus voltage supply for RSC to work normally, the GSC is responsible for maintaining steady DC-bus voltage, achieving high-quality three-phase current inputs, and adjusting the power factor.

With the installation of DC-link capacitors, decoupled control of RSC and GSC can be accomplished. For the proposed control strategy of the FSTP converter, the upper and lower capacitor voltages are separately measured, and they are utilized in the simplified SVPWM process. In addition, voltage balancing is achieved by feeding back the instantaneous DC current component in Phase A' to generate the compensating dq current components in the modified GSC control process. Moreover, as the information of the rotor speed and position is missing due to the failure of the speed/position encoder, the EKF estimator is applied in the sensorless control process to estimate the rotor speed and position. The overall control block diagram of the FSTP BTB converter-based DFIG-WT without the speed/position encoder is displayed in Figure 7.

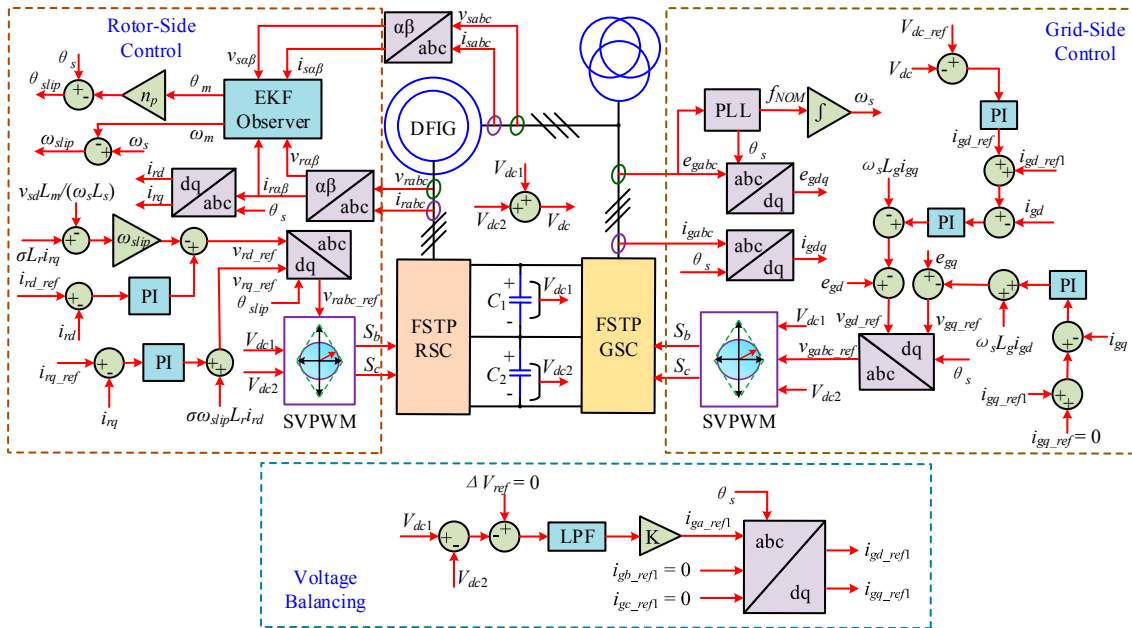


Figure 7. Control block diagram of the FSTP converter-based DFIG-WT by using the EKF estimator. GSC, grid-side converter; LPF, low-pass filter; SVPWM, space vector pulse width modulation.

5.1. RSC Controller Design

In order to accomplish maximum power point tracking (MPPT) for the DFIG WECS with VSCF operation as the precondition, effective control of the rotor speed ω_m and output active power P_t is the primary target. As the secondary purpose, which is ensuring the stability of the normal operation of grid-connected DFIG-WT, the output reactive power Q_t should be precisely controlled. The output active and reactive power output is strongly related to the dq components of the rotor currents, and the design of the RSC controller should be completed based on the control of the rotor currents.

The major part of the output power is from the stator side, and the power control is realized by controlling the operation of FSTP RSC. The stator active power output P_s contains the stator copper losses P_{cus} and stator output electromagnetic power P_{es} , which can be expressed as shown below.

$$P_s = P_{cus} + P_{es} = \text{Re}\left(\frac{3}{2}\mathbf{U}_s \widehat{\mathbf{I}}_s\right) + \frac{3}{2}\text{Re}(j\omega_s \boldsymbol{\varphi}_s \widehat{\mathbf{I}}_s), \quad (42)$$

The stator output reactive power Q_s is calculated as:

$$Q_s = \frac{3}{2}I_m(\mathbf{U}_s \widehat{\mathbf{I}}_s) \approx -\frac{3}{2}I_m(j\omega_s \boldsymbol{\varphi}_s \widehat{\mathbf{I}}_s) = \frac{3}{2}\text{Re}(\omega_s \boldsymbol{\varphi}_s \widehat{\mathbf{I}}_s), \quad (43)$$

According to (42) and (43) and with the negligence of the stator resistance R_s , the values of P_s and Q_s are derived as:

$$\begin{cases} P_s = \frac{3L_m}{2L_s} v_s di_{rd} \\ Q_s = -\frac{3v_{sd}}{2\omega_s L_s} (v_{sd} + \omega_s L_m i_{rq}) \end{cases} \quad (44)$$

The three-phase grid voltages are applied in the orientation of the dq axis, in which case the stator fluxes in the dq frame are obtained as:

$$\begin{cases} \varphi_{sd} \approx 0 \\ \varphi_{sq} \approx -\frac{E_m}{\omega_s} \end{cases} \quad (45)$$

The rotor fluxes can be expressed by the following equations.

$$\begin{cases} \varphi_{rd} = \sigma L_r i_{rd} \\ \varphi_{rq} = -\frac{L_m E_m}{\omega_s L_s} + \sigma L_r i_{rq} \end{cases} \quad (46)$$

Considering the steady operation of DFIG and neglecting the dynamic process caused by stator field currents, the rotor dq voltages are derived as:

$$\begin{cases} v_{rd} = R_r i_{rd} + \sigma L_r \frac{di_{rd}}{dt} - \omega_{slip} \varphi_{rq} \\ v_{rq} = R_r i_{rq} + \sigma L_r \frac{di_{rq}}{dt} + \omega_{slip} \varphi_{rd} \end{cases} \quad (47)$$

By substituting (46) into (47), the following equations are obtained.

$$\begin{cases} v_{rd} = R_r i_{rd} + \sigma L_r \frac{di_{rd}}{dt} - \omega_{slip} \left(-\frac{L_m E_m}{\omega_s L_s} + \sigma L_r i_{rq} \right) \\ v_{rq} = R_r i_{rq} + \sigma L_r \frac{di_{rq}}{dt} + \omega_{slip} \sigma L_r i_{rd} \end{cases} \quad (48)$$

Following (48), the current control loop in rotor-side control is drawn as shown in Figure 7.

5.2. GSC Controller Design

There are two loops in the control process of GSC, which are the outer voltage loop and the inner current loop. In the outer voltage loop, a steady DC-bus voltage is to be kept, while the current waveform quality and power factor are related to the control performance of the inner current control loop. The dual-loop control structure is displayed in Figure 8.

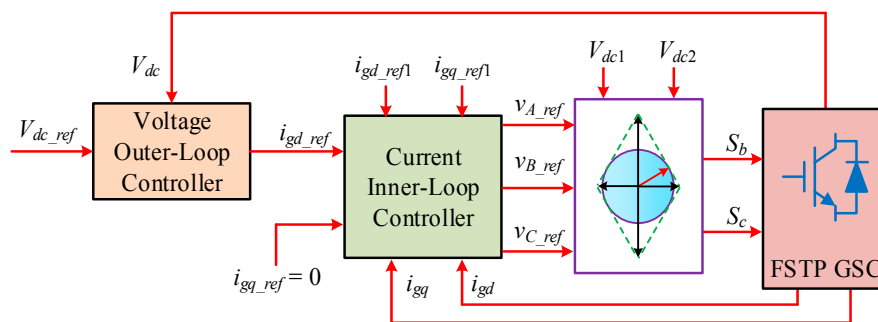


Figure 8. Dual control loop structure for FSTP GSC.

The three-phase AC voltages on GSC in dq reference frame can be derived as:

$$\begin{cases} v_{gd} = e_{gd} - R_g i_{gd} - L_g \frac{di_{gd}}{dt} + \omega_s L_g i_{gq} \\ v_{gq} = -R_g i_{gq} - L_g \frac{di_{gq}}{dt} - \omega_s L_g i_{gd} \end{cases} \quad (49)$$

In the controller design process for FSTP GSC, the compensating dq current components i_{gd_ref1} and i_{gq_ref1} are taken into account in order to eliminate the voltage deviation between the upper and lower capacitor voltages, and the design of GSC controller is illustrated by:

$$\begin{cases} L_g \frac{di_{gd}}{dt} = L_g \frac{di_{gd_ref1}}{dt} + K_{pd}(i_{gd_ref} + i_{gd_ref1} - i_{gd}) + K_{id} \int (i_{gd_ref} + i_{gd_ref1} - i_{gd}) dt \\ L_g \frac{di_{gq}}{dt} = L_g \frac{di_{gq_ref1}}{dt} + K_{pq}(i_{gq_ref} + i_{gq_ref1} - i_{gq}) + K_{iq} \int (i_{gq_ref} + i_{gq_ref1} - i_{gq}) dt \end{cases}, \quad (50)$$

where K_{pd} , K_{id} are the proportional and integral gains for the controller of the d -axis grid-side current i_{gd} ; K_{pq} , K_{iq} are the proportional and integral gains for the controller of the q -axis grid-side current i_{gq} .

5.3. Voltage Balancing at the DC-Bus Midpoint

The design of the control loop for eliminating the DC-link capacitor voltage deviation is based on (36), from which it can be seen that if the DC-link capacitance C_{DC} is large enough, the fluctuation in the voltage difference can be omitted. In practice, it is not possible to use an extremely large value of C_{DC} due to the limited space in the converter and the strict requirement on cost-effectiveness. Nevertheless, by extracting the low-frequency components in i_{ga} , the compensation in the steady-state error between the upper and lower capacitor voltages is derived, which is realized by using a low-pass filter (LPF).

The values of controller gains are listed in Table 4.

Table 4. Controller gains.

Controller Type	DC-Bus Voltage Controller	GSC Current Controller	RSC Current Controller	DC-Link Voltage Balancing Controller
Proportional Gain	0.5	15	0.6	0.16
Integral Gain	130	1500	8	0

6. Simulation Results

To verify the proposed fault-tolerant strategy by using FSTP converters and the EKF estimator-based sensorless control scheme for a late-stage DFIG-WT with hybrid faults of converter bridge arm open circuit and speed/position sensor failure, simulation studies are carried out in MATLAB/Simulink2017a (MathWorks, Natick, MA, USA). A 1.5-MW DFIG-WT is studied in the simulation, and the initial rotor speed is set as 1.2 pu, with the initial rotor position equal to zero, and the sampling time T_s is set as 5 μ s. The system parameters for the 1.5-MW DFIG-WT are shown in Table 5.

Table 5. Parameters of DFIG-WT.

Parameter	Value	Unit
Rated Power S_g	1.5	MVA (mega volt-ampere)
Rated Frequency F_{nom}	50	Hz
Rated Stator Voltage V_s	575	V
Stator Resistance R_s	0.023	pu
Rotor Resistance R_r	0.016	pu
Stator Inductance L_{ls}	0.18	pu
Rotor Inductance L_{lr}	0.16	pu
Magnetizing Inductance L_m	2.9	pu
Friction Factor F	0.01	pu
Inertia Constant H	6.85	s
Number of Pole Pairs n_p	3	\
DC Bus Capacitance C_{DC}	10	mF
Rated Wind Speed v_w	11	m/s

By directly taking the uncertainties in the stochastic process into account and calculating the Kalman gain matrix $K(k)$ online to minimize the errors, the unmeasured state variables can be precisely estimated by adopting the EKF algorithm as an estimator in a nonlinear system. In the seventh-order DFIG model, the mechanical variables are to be estimated since only the electrical variables are available as the inputs and measurements. In the proposed sensorless control process, the rotor angular speed ω_m and position θ_m are estimated to replace the conventional speed/position encoder. Assuming the wind speed is 15 m/s, the real and estimated rotor angular speeds and positions are respectively depicted in Figures 9 and 10, along with the error between the real and estimated values.

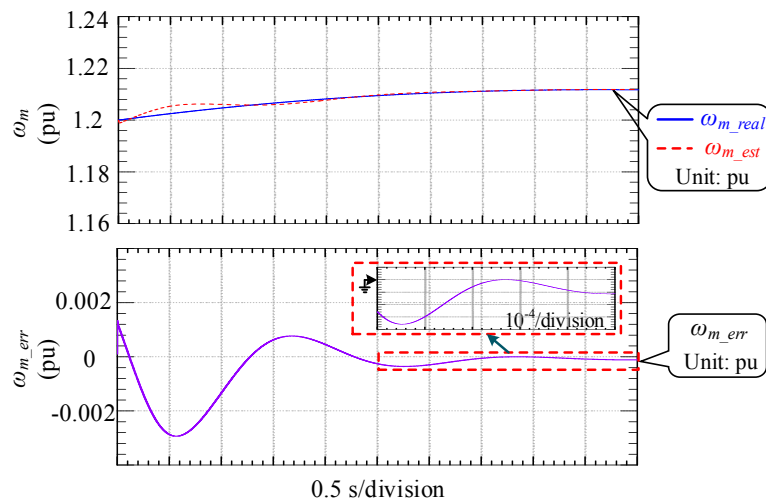


Figure 9. Real and estimated rotor angular speeds and the estimation error by using the EKF algorithm when wind speed = 15 m/s.

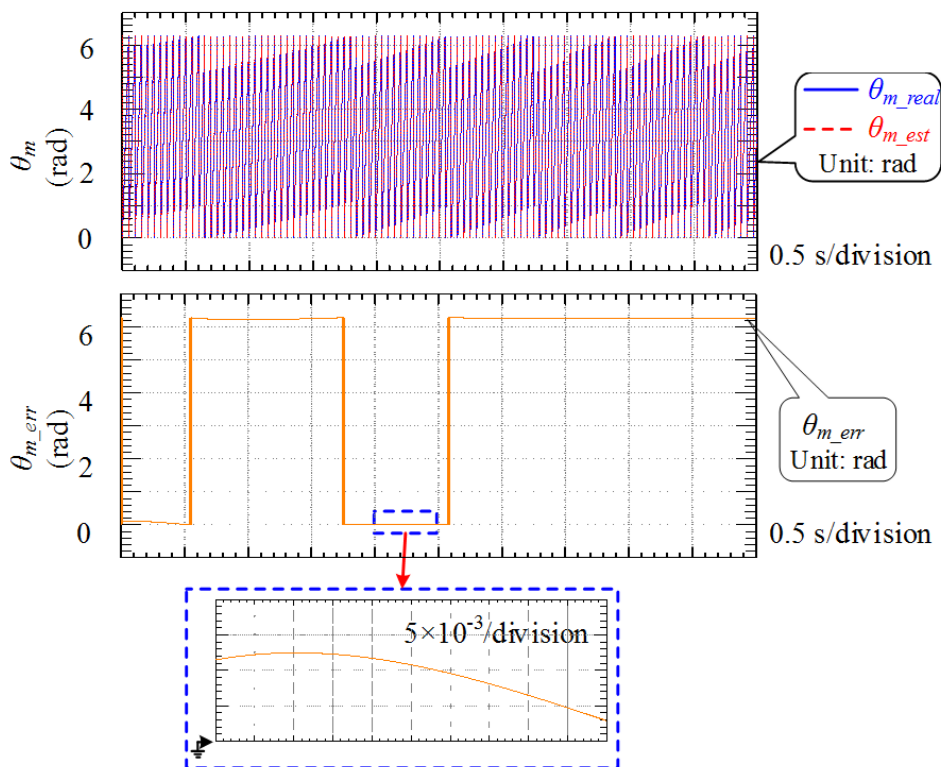


Figure 10. Real and estimated rotor positions and the estimation error by using the EKF algorithm when wind speed = 15 m/s.

From Figure 9, it can be seen that the error between the real and estimated rotor angular speeds constantly decreases and the estimation precision is extremely high after 2.5 s, where the error is in the order of 10^{-4} pu. For the estimation of rotor position, which is displayed in Figure 10, the estimated value tracks the real one very well, and the error is in the order of 5×10^{-3} rad. Since the rotor angle is limited in the range of $[0, 2\pi]$, there are some points where the estimation error reaches around 2π , which is caused by the fact that the estimated value lags the real one by a small time step.

In practice, the wind speed changes from time to time, and the operation of DFIG-WT has to be adjusted so that the highest wind energy conversion efficiency can be derived. The wind speed fluctuation between 7 m/s and 15 m/s is considered to verify that the post-fault DFIG-WT with the proposed hybrid fault-tolerant strategies can stay connected to the grid and continuously provide reliable electrical power output. The wind speed fluctuations are displayed in Figure 11.

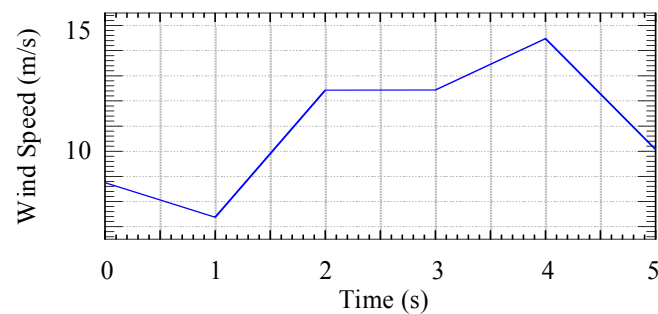


Figure 11. Wind speed fluctuation between 7 m/s and 15 m/s.

The unique feature of the EKF sensorless control algorithm is that it has strong robustness to the white noises induced in the system modelling process and measurements, which is the reason why it is widely used as an efficient estimator for system state variables regardless of its computational complexity. Along with the wind speed fluctuation between 7 m/s and 15 m/s, the white noises that obey a Gaussian distribution in the measurements are introduced at $t = 0.1$ s, with the noise covariance matrix given as $\mathbf{N} = [10^{-4}; 10^{-4}; 10^{-4}; 10^{-4}]^T$ (unit: pu). The estimation results under this circumstance are displayed in Figures 12 and 13, respectively.

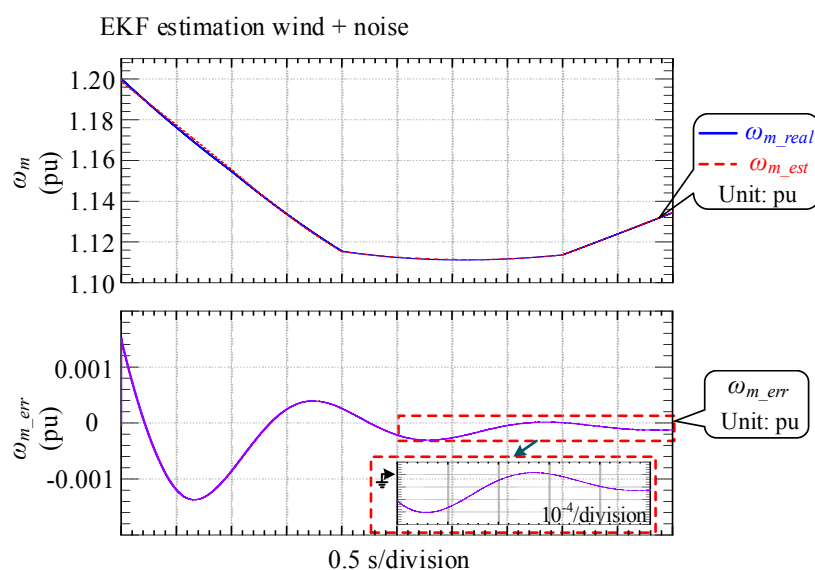


Figure 12. Real and estimated rotor angular speeds and the estimation error by using the EKF algorithm with wind speed fluctuation and measurement white noises injected at $t = 0.1$ s.

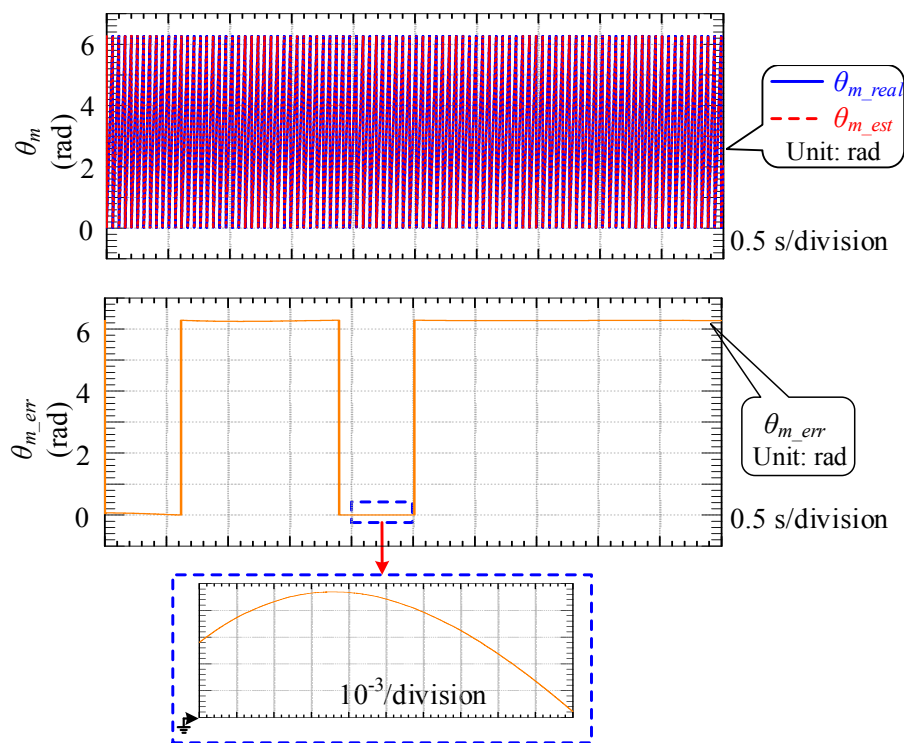


Figure 13. Real and estimated rotor positions and the estimation error by using the EKF algorithm with wind speed fluctuation and measurement white noises injected at $t = 0.1$ s.

By comparing the results derived in Figures 12 and 13 with those in Figures 9 and 10, the precision of estimation remains at the same level, which fully demonstrates the reliability of the proposed EKF algorithm for sensorless control of DFIG, and the estimated rotor angular speed and position can be directly applied in the overall control process to eliminate the speed/rotor encoder.

In order to effectively control the DFIG-WT by regulating the active and reactive power through controlling RSC, it is significant that the DC-bus voltage is maintained at an almost fixed value, which is realized in the voltage control process of GSC. Additionally, the harmonic components in the grid-side output three-phase currents should be reduced to ensure the high quality of power generation. Besides, the output power factor is also controlled to be unity. By using FSTP GSC in the post-fault operation, the aforementioned targets can be met, and the simulation results for the DC-bus voltage V_{dc} , three-phase GSC currents i_{gabc} , three-phase total output currents i_{tabc} and the output power factor with wind speed fluctuation are displayed in Figure 14.

From Figure 14, it can be seen that the DC-bus voltage is almost maintained at 1.8 kV, which is around two-times the value when an SSTP is used in the normal case. In terms of the quality of three-phase currents, nearly sinusoidal waveforms are presented at the output terminal. Although the distortions in the three-phase GSC currents i_{gabc} are obviously observed, they do not deteriorate the overall quality of the output three-phase currents too much. From Figure 14d, the output power factor is almost maintained at unity during the whole process, demonstrating relatively good resilience of the FSTP GSC. The performance of the FSTP RSC is illustrated by the total output active and reactive power, and the kinetic characteristic is revealed by the mechanical torque T_m and electromagnetic torque T_{em} . The plots of output power and torque are shown in Figure 15.

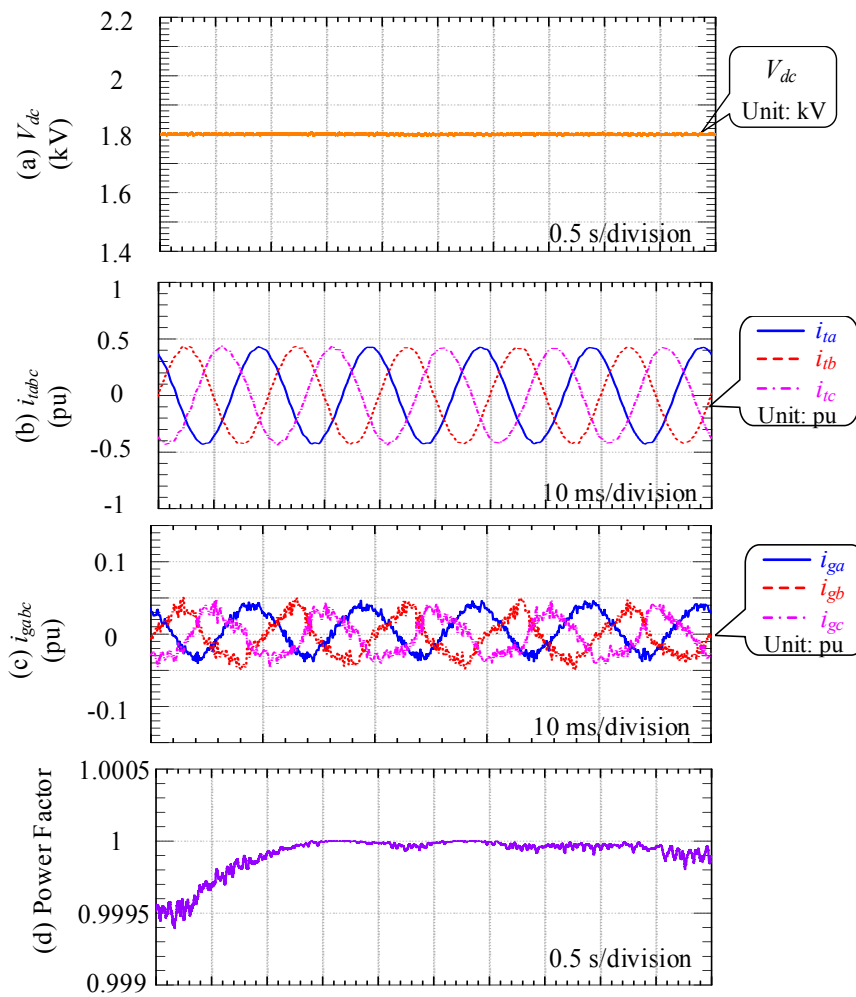


Figure 14. (a) DC-bus voltage V_{dc} ; (b) three-phase GSC currents i_{abc} ; (c) three-phase total output currents i_{gabc} ; and (d) the output power factor with wind speed fluctuation.

From Figure 15, the total active power output P_t changes due to the continuous variations in the mechanical torque. The electromagnetic torque T_{em} follows the mechanical torque value to keep the rotor speed constant, as can be seen from Figure 15c. In addition, appropriate control of the reactive power Q_t is achieved.

To further demonstrate the validity of the proposed hybrid fault-tolerant strategy with the FSTP BTB converter and the EKF sensorless control algorithm, a three-phase grid voltage sag is applied at $t = 1.2$ s, and the three-phase grid voltage amplitude decreases to half of the original value; it ends at $t = 1.3$ s. The three-phase grid voltages in this case are displayed in Figure 16.

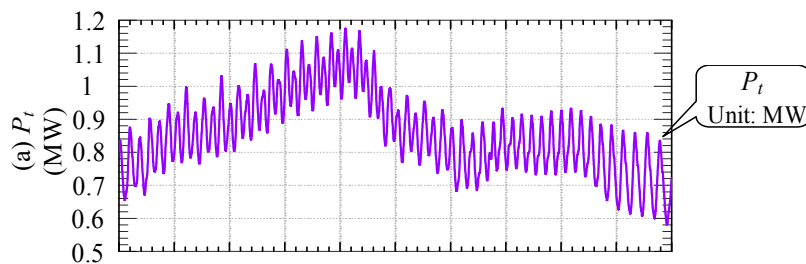


Figure 15. Cont.

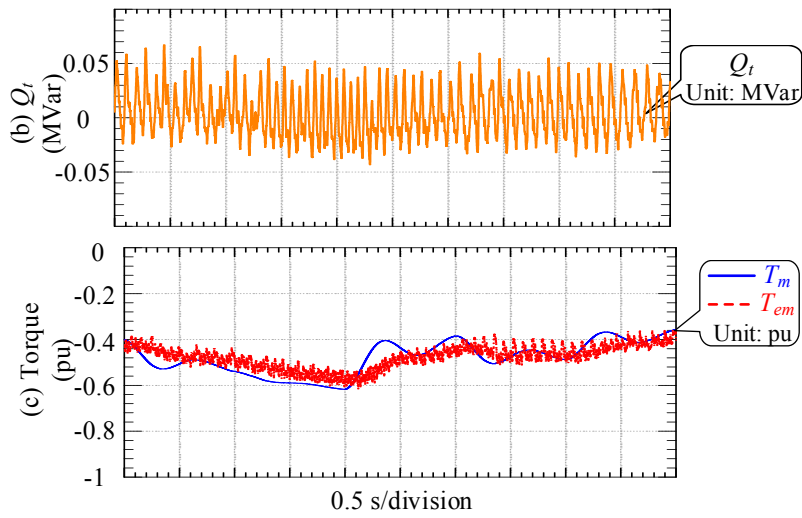


Figure 15. (a) Output active power P_t ; (b) output reactive power Q_t ; and (c) the mechanical torque T_m and electromagnetic torque T_{em} with wind speed fluctuation.

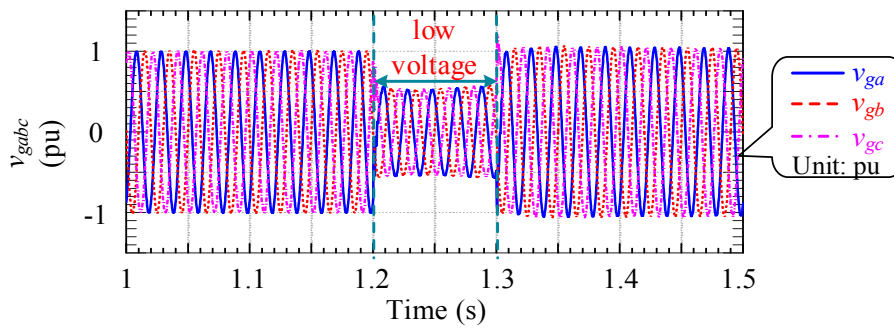


Figure 16. Three-phase grid voltages with a low voltage period from $t = 1.2$ s–1.3 s.

The simulation results with respect to those in Figures 14 and 15 by considering the wind speed fluctuation and grid voltage sag are presented in Figures 17 and 18, respectively.

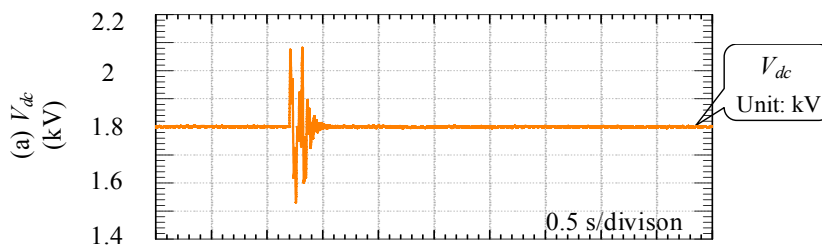


Figure 17. Cont.

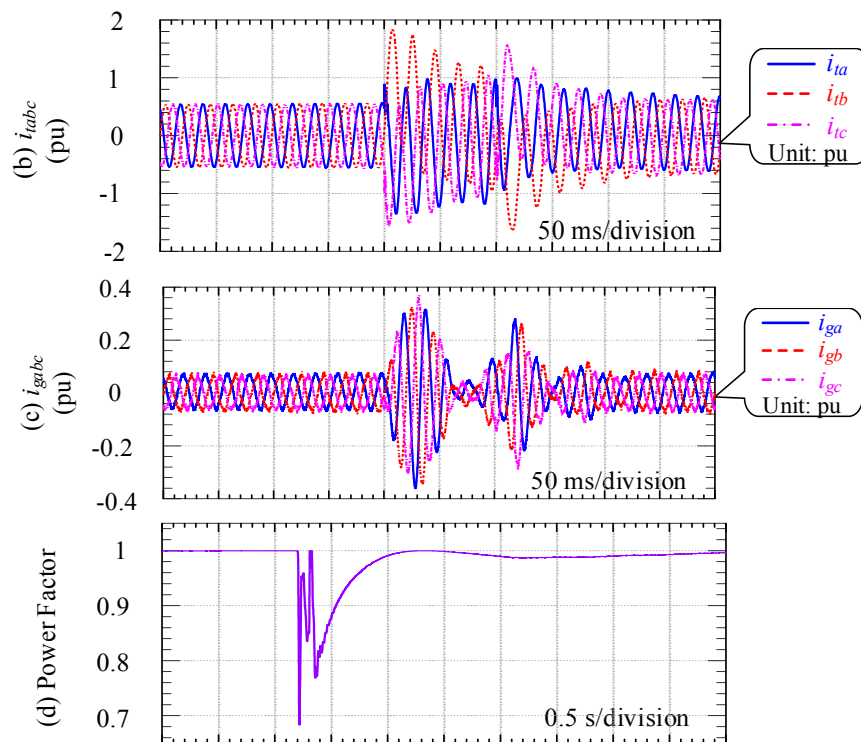


Figure 17. (a) DC-bus voltage V_{dc} ; (b) three-phase GSC currents i_{gabc} ; (c) three-phase total output currents i_{tabc} ; and (d) the output power factor with wind speed fluctuation.

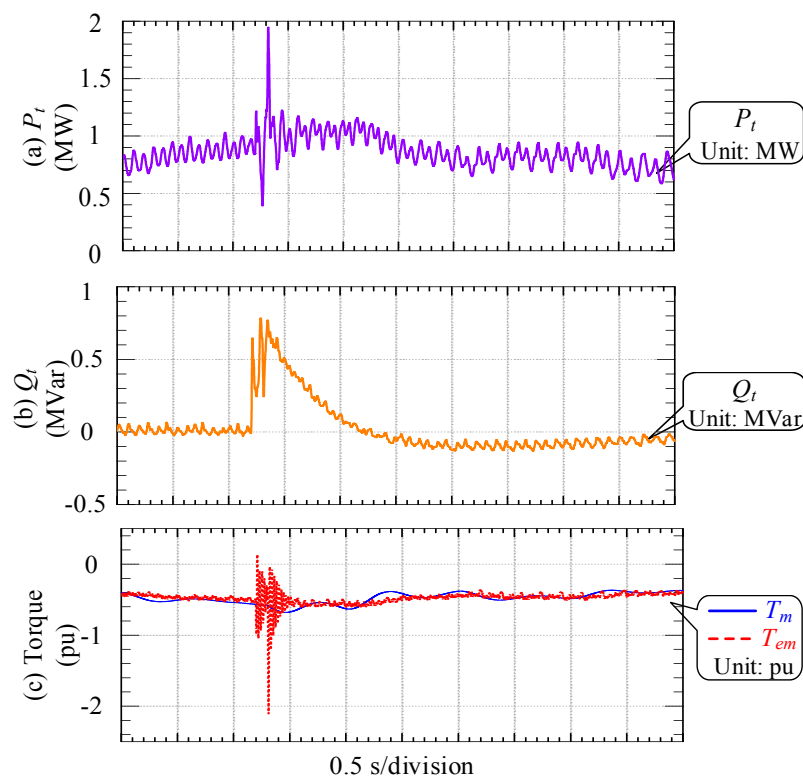


Figure 18. (a) Output active power P_t ; (b) output reactive power Q_t ; and (c) the mechanical torque T_m and electromagnetic torque T_{em} with wind speed fluctuation.

From the simulation results shown in Figures 17 and 18, some fluctuations in the variables are induced during and after the low voltage period. Especially for the power factor, the lowest value reaches 0.7 at around 1.2 s, and the value of the total output reactive power Q_t during the low voltage period is large. However, the proper control of active and reactive power output can still be obtained after 2.5 s, and the power factor returns to unity. Furthermore, the output three-phase current waveforms are almost sinusoidal after the low voltage period, and relatively good current quality for i_{gabc} is derived. More specifically, the total harmonic distortion (THD) of i_{tabc} and that of i_{gabc} are shown in Table 6.

Table 6. Total harmonic distortion (THD) of three-phase currents.

Phase Current	Magnitude of Fundamental (50 Hz) Component	THD
i_{ta}	0.4574	1.69%
i_{tb}	0.4584	2.49%
i_{tc}	0.4569	2.32%
i_{ga}	0.04696	12.39%
i_{gb}	0.04741	22.54%
i_{gc}	0.04537	22.22%

Although the THDs in the three-phase GSC currents are relatively large, the overall quality of the three-phase output currents is not affected greatly, and there is little distortion in the current of each phase. Therefore, with wind speed fluctuation and grid voltage sag, the FSTP GSC can still work properly to keep high-quality power output. Moreover, the balance between the upper and lower DC-link capacitor voltages can be achieved by using the proposed voltage balancing scheme, which maximizes the DC-bus voltage utilization rate. The upper and lower capacitor voltages with and without the low voltage period are displayed in Figure 19, and the voltage difference is illustrated in Figure 20 for each case.

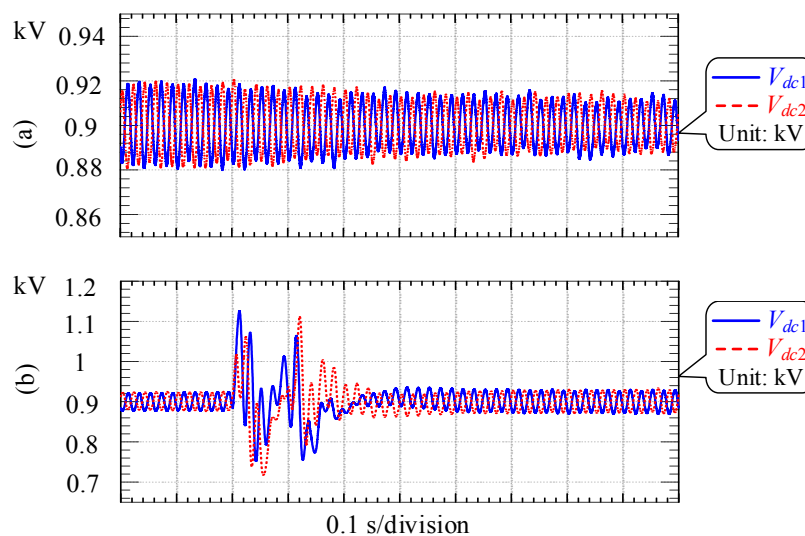


Figure 19. Upper and lower capacitor voltages (a) without the low voltage period and (b) with the low voltage period from $t = 1.2$ s–1.3 s.

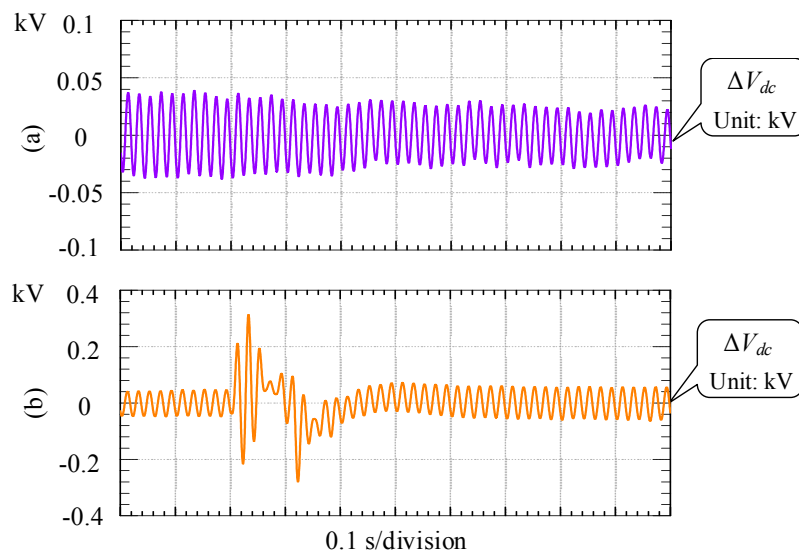


Figure 20. Upper and lower capacitor voltage difference (a) without the low voltage period and (b) with the low voltage period from $t = 1.2$ s–1.3 s.

It can be seen from Figures 19 and 20 that the steady-state error between V_{dc1} and V_{dc2} is small either for the case with or without the low voltage period inserted. From Figures 19b and 20b, the fluctuations in the capacitor voltages and the difference are large during the low voltage period, while the voltage values return to the normal level instantly after the grid voltage sag is removed. For both situations, the voltage deviation between V_{dc1} and V_{dc2} is generally within 40 V, which verifies the effectiveness of the voltage balancing scheme.

7. Conclusions

This paper discusses the hybrid fault scenario with open-circuit faults in the BTB converter and rotor speed/position encoder failure in late-stage offshore DFIG-WT. Based on the seventh-order DFIG dynamic state space model, the EKF estimator is designed to estimate the rotor speed and position, with the stator and rotor voltages/currents applied as the inputs and measurements of the system. In order to ride through the converter open-circuit fault without increasing the circuit complexity, an FSTP topology-based BTB fault-tolerant converter is utilized. A simplified SVPWM technique and DC voltage balancing scheme are proposed to reduce the computational burden and increase the DC-bus voltage utilization rate, respectively.

From the simulation results, the following key points are derived.

- (1) Precise estimations of the rotor angular speed and position can be derived, even when wind speed fluctuation and measurement noises are taken into account.
- (2) Steady DC-bus voltage, high-quality three-phase output current waveforms and the unity power factor can be achieved by using FSTP GSC when wind speed fluctuation and grid voltage sag are included.
- (3) Proper control of active and reactive output power can be derived by employing FSTP RSC under harsh operating environments.
- (4) The DC-link capacitor voltages are well balanced by considering the wind speed fluctuation and grid voltage sag.

Author Contributions: Wei Li wrote the paper and did the simulations. Gengyin Li supervised the first author in writing the paper and doing the simulations. Kai Ni provided technical support and revised the language. Yihua Hu checked the logic of the paper and gave some comments on revising the paper. Xinhua Li collected some materials for the background of this study.

Conflicts of Interest: The authors declare no conflict of interest.

Nomenclature

v, e, i, φ	Instantaneous values of voltage, source voltage, current and flux
V_{dc}, V_{dc1}, V_{dc2}	DC-link voltage, upper and lower capacitor voltages
E_m, V_m, I_m	Amplitudes of the three-phase source voltages, converter voltages and currents
ΔV	Voltage difference ($\Delta V = V_{dc2} - V_{dc1}$)
R	Resistance
L_m, L_{ls}, L_{lr}	Mutual inductance, stator leakage inductance and rotor leakage inductance
L_g, L_s, L_r	Inductances on the grid, stator and rotor ($L_s = L_m + L_{ls}$; $L_r = L_m + L_{lr}$)
σ	Leakage coefficient ($\sigma = 1 - (L_m^2 / L_s L_r)$)
C_1, C_2, C_{DC}	Upper capacitance, lower capacitance and DC-link capacitance
P, Q	Active and reactive power
$d_{00}, d_{10}, d_{11}, d_{01}$	Duty ratios of active time for voltage vectors $V_{00}, V_{10}, V_{11}, V_{01}$
d_b, d_c	Duty ratios of active time for the switching functions S_b and S_c
m	Modulation index
f_{NOM}	Nominal grid frequency
$\theta_s, \theta_m, \theta_{slip}$	Synchronous, rotor and slip angular positions
n_p	Number of pole pairs
s	Slip
$\omega_s, \omega_{slip}, \omega_m$	Nominal grid angular frequency, slip angular frequency, electrical rotor angular speed
T_s, T_{sw}	Sampling time and switching time
PLL, LPF	Phase locked loop, low-pass filter
<u>Subscripts</u>	
s, r, g, t	Stator, rotor, grid, total
$a, b, c; A, B, C$	Phases A, B, C; Points A, B, C
$\alpha, \beta; d, q$	Direct and quadrature components referred to the stationary/synchronous reference frame
$_{ref}, _{ref1}$	Reference value, transient DC reference value
$C1, C2$	Upper and lower capacitors
<u>Superscripts</u>	
$*, \hat{\cdot}, \sim, T$	Ideal value, estimated value, conjugate and transpose

References

1. Tan, Y.; Muttaqi, K.M.; Ciufu, P.; Meegahapola, L. Enhanced Frequency Response Strategy for a PMSG-Based Wind Energy Conversion System Using Ultracapacitor in Remote Area Power Supply Systems. *IEEE Trans. Ind. Appl.* **2017**, *53*, 549–558. [[CrossRef](#)]
2. Sanusi, W.; al Hosani, M.; Moursi, M.S.E. A Novel DC Fault Ride-Through Scheme for MTDC Networks Connecting Large-Scale Wind Parks. *IEEE Trans. Sustain. Energy* **2017**, *8*, 1086–1095. [[CrossRef](#)]
3. Saleh, S.A.; Meng, R.; McSheffery, R. Evaluating the Performance of Digital Modular Protection for Grid-Connected Permanent-Magnet-Generator-Based Wind Energy Conversion Systems with Battery Storage Systems. *IEEE Trans. Ind. Appl.* **2017**, *53*, 4186–4200. [[CrossRef](#)]
4. Andalib-Bin-Karim, C.; Liang, X.; Khan, N.; Zhang, H. Determine Q–V Characteristics of Grid-Connected Wind Farms for Voltage Control Using a Data-Driven Analytics Approach. *IEEE Trans. Ind. Appl.* **2017**, *53*, 4162–4175. [[CrossRef](#)]
5. Lu, B.; Li, Y.; Wu, X.; Yang, Z. A Review of Recent Advances in Wind Turbine Condition Monitoring and Fault Diagnosis. In Proceedings of the Power Electronics and Machines in Wind Applications, Lincoln, NE, USA, 24–26 June 2009.
6. Lee, T.-S.; Liu, J.-H. Modeling and Control of a Three-Phase Four-Switch PWM Voltage-Source Rectifier in d-q Synchronous Frame. *IEEE Trans. Power Electron.* **2011**, *26*, 2476–2489. [[CrossRef](#)]
7. Genduso, F.; Cecati, C.; di Tommaso, A.O.; Miceli, R.; Galluzzo, G.R. Comprehensive Modelling and Experimental Testing of Fault Detection and Management of a Non-Redundant Fault-Tolerant VSI. *IEEE Trans. Ind. Electron.* **2015**, *62*, 3945–3954. [[CrossRef](#)]

8. Zeng, Z.; Zheng, W.; Zhao, R.; Zhu, C.; Yuan, Q. The Comprehensive Design and Optimization of the Post-Fault Grid-Connected Three-Phase PWM Rectifier. *IEEE Trans. Power Electron.* **2016**, *63*, 1629–1642. [[CrossRef](#)]
9. Zeng, Z.; Zheng, W.; Zhao, R.; Zhu, C.; Yuan, Q. Modeling, Modulation and Control of the Three-Phase Four-Switch PWM Rectifier under Balanced Voltage. *IEEE Trans. Power Electron.* **2016**, *31*, 4892–4905. [[CrossRef](#)]
10. Zeng, Z.; Zheng, W.; Zhao, R. Performance Analysis of the Zero-Voltage Vector Distribution in Three-Phase Four-Switch Converter Using a Space Vector Approach. *IEEE Trans. Power Electron.* **2017**, *32*, 260–273. [[CrossRef](#)]
11. Zhou, D.; Zhao, J.; Liu, Y. Predictive Torque Control Scheme for Three-Phase Four-Switch Inverter-Fed Induction Motor Drives With DC-Link Voltages Offset Suppression. *IEEE Trans. Power Electron.* **2015**, *30*, 3309–3318. [[CrossRef](#)]
12. Zaky, M.S.; Metwaly, M.K. A Performance Investigation of a Four-Switch Three-Phase Inverter-Fed IM Drives at Low Speeds Using Fuzzy Logic and PI Controllers. *IEEE Trans. Power Electron.* **2017**, *32*, 3741–3753. [[CrossRef](#)]
13. Lee, B.-K.; Kim, T.-H.; Ehsani, M. On the Feasibility of Four-Switch Three-Phase BLDC Motor Drives for Low Cost Commercial Applications: Topology and Control. *IEEE Trans. Power Electron.* **2003**, *18*, 164–172.
14. Masmoudi, M.; Badsì, B.E.; Masmoudi, A. DTC of B4-Inverter-Fed BLDC Motor Drives with Reduced Torque Ripple During Sector-to-Sector Commutations. *IEEE Trans. Power Electron.* **2014**, *29*, 4855–4865. [[CrossRef](#)]
15. Freire, N.M.A.; Cardoso, A.J.M. Fault-Tolerant PMSG Drive with Reduced DC-Link Ratings for Wind Turbine Applications. *IEEE J. Emerg. Sel. Top. Power Electron.* **2014**, *2*, 26–34. [[CrossRef](#)]
16. Freire, N.M.A.; Cardoso, A.J.M. A Fault-Tolerant Direct Controlled PMSG Drive for Wind Energy Conversion Systems. *IEEE Trans. Power Electron.* **2014**, *61*, 821–834. [[CrossRef](#)]
17. Freire, N.M.A.; Cardoso, A.J.M. A Fault-Tolerant PMSG Drive for Wind Turbine Applications with Minimal Increase of the Hardware Requirements. *IEEE Trans. Ind. Appl.* **2014**, *50*, 2039–2049. [[CrossRef](#)]
18. Ni, K.; Hu, Y.; Liu, Y.; Gan, C. Fault-Tolerant Operation of DFIG-WT With Four-Switch Three-Phase Grid-Side Converter by Applying A Simplified SVPWM Technique. In Proceedings of the 2017 IEEE International Electrical Machines and Drives Conference (IEMDC), Miami, FL, USA, 21–24 May 2017.
19. Ni, K.; Hu, Y.; Liu, Y.; Gan, C. Performance Analysis of a Four-Switch Three-Phase Grid-Side Converter with Modulation Simplification in a Doubly-Fed Induction Generator-Based Wind Turbine (DFIG-WT) with Different External Disturbances. *Energies* **2017**, *10*, 706. [[CrossRef](#)]
20. Alsofyani, I.M.; Idris, N.R.N. A review on sensorless techniques for sustainable reliability and efficient variable frequency drives of induction motors. *Renew. Sustain. Energy Rev.* **2013**, *24*, 111–121. [[CrossRef](#)]
21. Holtz, J. Sensorless Control of Induction Machines: With or Without Signal Injection? *IEEE Trans. Power Electron.* **2006**, *53*, 7–30. [[CrossRef](#)]
22. Frus, J.R.; Kuo, B.C. Closed-loop control of step motors using waveform detection. In Proceedings of the International Conference Stepping Motors and Systems, Leeds, UK, 13–15 July 1976.
23. Auger, F.; Hilairet, M.; Guerrero, J.M.; Monmasson, E.; Orłowska-Kowalska, T.; Katsura, S. Industrial Applications of the Kalman Filter: A Review. *IEEE Trans. Power Electron.* **2013**, *60*, 5458–5471. [[CrossRef](#)]
24. Simon, D. *Optimal State Estimation: Kalman, H_∞ , and Nonlinear Approaches*; Wiley: Hoboken, NJ, USA, 2006.
25. Grewal, M.; Andrews, A. *Kalman Filtering: Theory and Practice Using MATLAB*; Wiley-IEEE Press: New York, NY, USA, 2008.
26. Shi, K.L.; Chan, T.F.; Wong, Y.K.; Ho, S.L. Speed Estimation of an Induction Motor Drive Using an Optimized Extended Kalman Filter. *IEEE Trans. Power Electron.* **2002**, *49*, 124–133. [[CrossRef](#)]
27. Barut, M.; Bogosyan, S.; Gokasan, M. Speed-Sensorless Estimation for Induction Motors Using Extended Kalman Filters. *IEEE Trans. Power Electron.* **2007**, *54*, 272–280. [[CrossRef](#)]
28. Barut, M.; Bogosyan, S.; Gokasan, M. Experimental Evaluation of Braided EKF for Sensorless Control of Induction Motors. *IEEE Trans. Power Electron.* **2008**, *55*, 620–632. [[CrossRef](#)]
29. Alonge, F.; Cangemi, T.; D’Ippolito, F.; Fagiolini, A.; Sferlazza, A. Convergence Analysis of Extended Kalman Filter for Sensorless Control of Induction Motor. *IEEE Trans. Power Electron.* **2015**, *62*, 2341–2352. [[CrossRef](#)]
30. Maldonado, E.; Silva, C.E.; Olivares, M. Sensorless control of a doubly fed induction machine based on an Extended Kalman Filter. In Proceedings of the 2011 14th European Conference on Power Electronics and Applications, Birmingham, UK, 30 August–1 September 2011.

31. Perez, I.R.; Silva, J.C.; Yuz, E.J.; Carrasco, R.G. Experimental Sensorless Vector Control Performance of a DFIG Based on an Extended Kalman Filter. In Proceedings of the IECON 2012—38th Annual Conference on IEEE Industrial Electronics Society, Montreal, QC, Canada, 25–28 October 2012.
32. Malakar, M.K.; Tripathy, P.; Krishnaswamy, S. State Estimation of DFIG using an Extended Kalman Filter with an Augmented State Model. In Proceedings of the 2014 Eighteenth National Power Systems Conference (NPSC), Guwahati, India, 18–20 December 2014.
33. Serhoud, H.; Benattous, D. Sensorless optimal power control of brushless doubly-fed machine in wind power generator based on extended kalman filter. *Int. J. Syst. Assur. Eng. Manag.* **2013**, *4*, 57–66. [[CrossRef](#)]
34. Goodwin, G.; Yuz, J.; Aguero, J.C.; Cea, M. Sampling and sampleddata models. In Proceedings of the American Control Conference (ACC), Baltimore, MD, USA, 30 June–2 July 2010; pp. 1–20.
35. Yuz, J.; Goodwin, G. On sampled-data models for nonlinear systems. *IEEE Trans. Autom. Control* **2005**, *50*, 1477–1489. [[CrossRef](#)]
36. Silva, C.; Yuz, J. On sampled-data models for model predictive control. In Proceedings of the 2010 36th Annual Conference on IEEE Industrial Electronics Society (IECON), Glendale, AZ, USA, 7–10 November 2010; pp. 2966–2971.
37. Liu, Y.-C.; Ge, X.-L.; Zhang, J.; Feng, X.-Y. General SVPWM strategy for three different four-switch three-phase inverters. *Electron. Lett.* **2015**, *51*, 357–359. [[CrossRef](#)]



© 2017 by the authors. Licensee MDPI, Basel, Switzerland. This article is an open access article distributed under the terms and conditions of the Creative Commons Attribution (CC BY) license (<http://creativecommons.org/licenses/by/4.0/>).